

Clustering of photometric luminous red galaxies I : Growth of Structure and Baryon Acoustic Feature

M. Crocce^{1*}, E. Gaztañaga¹, A. Cabré², A. Carnero³, E. Sánchez³

¹*Institut de Ciències de l'Espai (IEEC-CSIC), Barcelona, Spain*

²*University of Pennsylvania, Philadelphia, USA*

³*Centro de Investigaciones Energéticas, Medioambientales y Tecnológicas (CIEMAT), Madrid, Spain*

11 November 2021

ABSTRACT

The possibility of measuring redshift space (RSD) distortions using photometric data have been recently highlighted. This effect complements and significantly alters the detectability of baryon acoustic oscillations (BAO) in photometric surveys. In this paper we present measurements of the angular correlation function of luminous red galaxies (LRGs) in the photometric catalog of the final data release (DR7) of the Sloan Digital Sky Survey II (SDSS). The sample compromise $\sim 1.5 \times 10^6$ LRGs distributed in $0.45 < z < 0.65$, with a characteristic photometric error of ~ 0.05 . Our measured correlation centered at $z = 0.55$ is in very good agreement with predictions from standard Λ CDM in a broad range of angular scales, $0.5^\circ < \theta < 6^\circ$. We find that the growth of structure can indeed be robustly measured, with errors matching expectations. The velocity growth rate is recovered as $f\sigma_8 = 0.53 \pm 0.42$ when no prior is imposed on the growth factor and the background geometry follows a Λ CDM model with WMAP7+SNiA priors. This is compatible with the corresponding General Relativity (GR) prediction $f\sigma_8 = 0.45$ for our fiducial cosmology. If we adopt a parameterization such that $f = \Omega_m^\gamma(z)$, with $\gamma \approx 0.55$ in GR, and combine our $f\sigma_8$ measurement with the corresponding ones from spectroscopic LRGs at lower redshifts we obtain $\gamma = 0.54 \pm 0.17$. In addition we find evidence for the presence of the baryon acoustic feature matching the amplitude, location and shape of Λ CDM predictions. The photometric BAO feature is detected with 98% confidence level at $z = 0.55$.

Key words: data analysis – cosmological parameters – dark energy – large-scale structure of the universe

1 INTRODUCTION

The discovery of an accelerated cosmic expansion has become one of the biggest puzzles in modern cosmology over the last 10 years. Several scientific probes have been proposed to understand the nature of this acceleration. From “geometrical” tests based on measurements of the distance-redshift relation such as baryon acoustic oscillations (BAO) or Type Ia supernovae, to “growth” tests sensitive to the growth rate of perturbations such as redshift space distortions (RSD), weak lensing or cluster abundance. The success of these probes relies in the implementation of massive, and many times dedicated, observational campaigns that will scan a good fraction of the observable Universe. Some such surveys will base their science in galaxy redshifts derived spectroscopically, what provides accurate radial positions.

Others will instead measure redshift photometrically. This yields poorer determination of radial positions but allows to go deeper in redshift and have higher sampling rate. The later group involves the Dark Energy Survey¹ (DES), the Physics of the Accelerating Universe collaboration² (PAU) and the Panoramic Survey Telescope and Rapid Response System³ (PanStarrs) as well as proposals such as the Large Synoptic Survey Telescope⁴ (LSST) and the imaging component of ESA/Euclid⁵ survey.

Perhaps the most exciting results related to the large scale structure of the Universe to date have been obtained using spectroscopic data from surveys such as the two degree

¹ www.darkenergysurvey.org

² www.pausurvey.org

³ pan-stars.ifa.hawaii.edu

⁴ www.lsst.org

⁵ www.euclid-imaging.net

* E-mail: martincrocce@gmail.com

field galaxy redshift survey (2dGRS, Colless et al. (2001)) the Sloan Digital Sky Survey (SDSS, York et al. (2000)) or the recent WiggleZ Dark Energy survey (Drinkwater et al. (2010)). This is particularly so in regards to redshift space distortions and baryon acoustic oscillations, the two topics of this paper.

Redshift space distortions arise because the receding speed of galaxies with respect to us is due not only to the Hubble expansion but also to their peculiar velocity. Hence, galaxy positions inferred with the Hubble law are modified with respect to their true positions depending on the local velocity field. At large scales the net effect results from the relative strength of the intrinsic clustering (the bias) and the amplitude of velocity flows set by the conservation of mass through the growth rate of structure parameter $f = \partial \ln D / \partial \ln a$ (where D is the linear growth factor and a the cosmological scale factor). Photometric redshift errors are generally assumed to wash out these distortions. As recently discussed by Nock et al. (2010) and Crocce et al. (2011) this is true to a good extent but does not remove the signal completely if one splits the data in redshift bins. Thus, RSD from photometric data could be a sensitive test for the growth of structure as a function of redshift (Ross et al. (2011)). This can then be used to discriminate modifications of Einstein's gravity from dark energy models.

In turn, BAO originate in the tight coupling between baryons and photons prior to recombination. At the time of decoupling their “last scattering” imprints a well defined comoving scale in the spatial distribution of baryons and matter of $\sim 100 h^{-1} \text{Mpc}$, characterized by a slight excess of pairs over random. This scale is today imprinted in the distribution of galaxies. Again, poor distance determination because of photometric redshift estimates wash out this excess, at least in the radial direction. Photometric surveys should still be capable of detecting this signature in the angular distribution of galaxies (e.g. Blake & Bridle (2005)).

In this paper we use the *angular correlation function* of luminous red galaxies (LRGs) in the imaging catalog of the final data release (DR7) of SDSS to address whether growth of structure can be robustly measured with photometric data despite several sources of systematic errors, low resolution photo-z and other unknowns. In parallel, we investigate whether BAO can be observed in the clustering pattern of LRGs in concordance with model predictions affected by redshift space distortions. In a companion paper, Carnero et al. (2011), we discuss the cosmological implications of the presence of BAO in the clustering signal.

These tests, that extend previous work using angular power spectrum (Padmanabhan et al. (2007); Blake et al. (2007); Thomas et al. (2011)), may serve as a proof-of-concept for the potential of future, more accurate, photometric data to place interesting constraints into the nature of cosmic expansion, and/or provide valuable higher redshift leverage to complement spectroscopic measurements.

This paper is organized as follows. In Sec. 2.1 we discuss our data, including the selection of the galaxy sample, survey mask and photo-z. In Sec. 3 we describe our angular correlation measurements including the error estimates and the impact of star contamination. Sec. 4 refers to our redshift space distortion analysis and the implications for the growth rate of structure. Sec. 5 is dedicated to discuss

the evidence for the baryon acoustic feature in the measured correlation. Lastly, Sec. 6 contains our main conclusions.

2 DATA

2.1 Selection of the Galaxy Sample

We perform a color based selection of LRGs in the photometric catalog of the final SDSS II data release (DR7, Abazajian et al. (2009)). We follow two main steps. The first one, based on that published by Cabré et al. (2006), aims at identifying the region in color-color space that is populated by high redshift LRGs (Eisenstein et al. (2001)) by selecting all those objects that verify

$$\begin{aligned} (r - i) &> \frac{(g - r)}{4} + 0.36, \\ (g - r) &> -0.72 (r - i) + 1.7, \end{aligned} \quad (1)$$

where the variables g, r, i are *model* magnitudes corrected by extinction. The second step is a set of cuts that are intended to minimize the star contamination in the sample,

$$\begin{aligned} 17 &< \textit{petror} < 21, \\ 0 &< \sigma_{\textit{petror}} < 0.5, \\ 0 &< r - i < 2, \\ 0 &< g - r < 3, \\ 22 &< \textit{mag}_{50} [\text{mag/arcsec}^2] < 24.5, \end{aligned} \quad (2)$$

where *petror* is petrosian magnitude (corrected by extinction), $\sigma_{\textit{petror}}$ is the error on *petror* and *mag*₅₀ is the surface brightness in magnitude *petror* at half-light radius r_{50} (the radius containing 50% of petrosian flux), $\textit{mag}_{50} = \textit{petror} + 2.5 \log(\pi r_{50}^2)$. These cuts yield a total of $\sim 1.27 \times 10^6$ objects with redshifts in the range ~ 0.4 to ~ 0.65 .

From the set of cuts in Eqs. (2) the first ones corresponds to our magnitude limits. The next ones ensure that colors correspond to a galaxy and effectively eliminates very few objects. Lastly the cut that is most effective, that in *mag*₅₀, with an upper bound on 24.5 to ensure well measured galaxies and a lower bound on 22 to eliminate bright point-like objects (i.e. stars). We have found that eliminating objects with $\textit{mag}_{50} > 24.5 \text{ mag/arcsec}^2$ leads to no difference in the clustering signal. However eliminating objects with $\textit{mag}_{50} < 22 \text{ mag/arcsec}^2$ reduces the amplitude of clustering at large scales by large factors even though they represents a small percentage of the total sample. Hence, we next discuss the motivation for this cut in more detail (further evidence for this effect is given in Sec. 3.2).

The distribution of *mag*₅₀ is given in Fig. 1. It is well concentrated around $\textit{mag}_{50} \sim 23 \text{ mag/arcsec}^2$ but shows long tails due to objects contaminating the LRG sample. This contamination is more clearly depicted in the *petror* vs. *mag*₅₀ diagram in Fig. 2. Top panel corresponds to our photometric sample and shows a different trend for $\textit{mag}_{50} < 22 \text{ mag/arcsec}^2$ and $\textit{mag}_{50} > 24.5 \text{ mag/arcsec}^2$, with the core of LRGs lying in between. Bottom panel shows the same diagram but for the SDSS DR7 spectroscopic sample, after imposing the selection in Eq. (1). This panel nicely shows that all objects with $\textit{mag}_{50} < 22 \text{ mag/arcsec}^2$ could be contaminated by stars. In addition, Fig. 3 shows a histogram of number of objects per pixel (here the pixel size

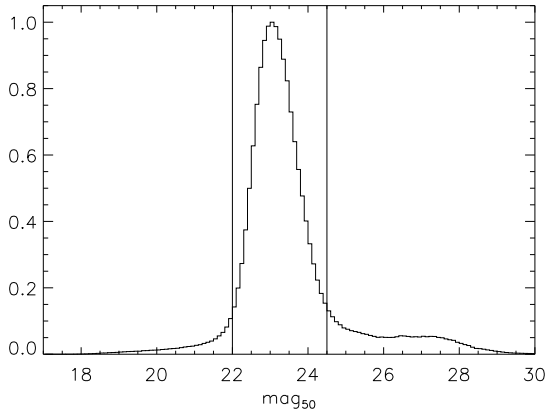


Figure 1. Histogram of surface brightness (mag_{50}) for all the objects in our catalog

is 0.01 deg^2) as a function of galactic latitude and different redshift bins, including (solid) or excluding (dashed) galaxies with low mag_{50} . Objects with low mag_{50} clearly concentrate at low galactic latitudes introducing artificial density gradients towards the galactic plane (which then results in large density fluctuations at large scales). There is a slight gradient residual after imposing the cut in mag_{50} , which we avoid but leaving out galactic latitudes (denoted b) lower than 25° . We require,

$$b \geq 25^\circ. \quad (3)$$

This yields a reduction of $\sim 3\%$ of the SDSS area used.

2.2 Angular Mask

We built the angular mask using a **Healpix** pixelization (Górski et al. (2005))⁶ over the entire sky with $N_{\text{side}} = 512$ that yields a pixel size of $\sim 0.01 \text{ deg}^2$.

We then eliminate from the analysis those pixels where the geometric acceptance of the survey is compatible with bad or no measurement by imposing a minimum number of galaxies per pixel (N/pixel) of 15. We notice that in order to build the mask we use *all* the objects in the photometric catalog (i.e. not limiting by $petror < 21$) because the density of LRGs is very low to allow a robust and well pixelized mask construction. In addition we look at galactic extinction and magnitude errors maps in order to mask badly observed regions. Figure 4 shows the distribution of errors in r-band magnitude averaged in every pixel (i.e. mean error per pixel) in the top panel, and in galactic extinction in the bottom panel. There is a clear correlation between these two quantities in regions of high extinction. Hence we suppress from our mask pixels with bad mean error rather than applying the cut directly to the LRG selection, as this would imply introducing artificially low density regions and corresponding systematic effects. In summary we discard pixels with extinction higher than 0.2 and mean error higher than 0.3. We have checked that using different pixelization sizes for the mask, as well as different levels of acceptance of a pixel

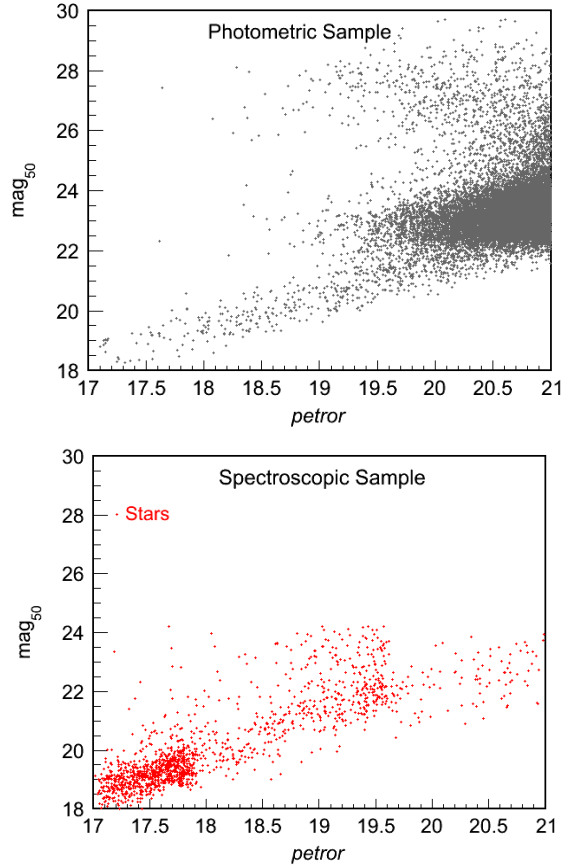


Figure 2. Surface brightness (mag_{50}) vs. Petrosian r apparent magnitude. Top panel corresponds to objects in our photometric LRG catalog, bottom panel to objects classified as stars in the SDSS DR7 spectroscopic sample that verifies the same selection as the top panel. Top panel shows some distinctive trends for $mag_{50} < 22 \text{ mag/arcsec}^2$ and for $mag_{50} > 24.5 \text{ mag/arcsec}^2$, which contaminate our sample and can modify the clustering signal. Bottom panels makes clear that the region of $mag_{50} < 22 \text{ mag/arcsec}^2$ is populated by stars. The region with $mag_{50} > 24.5 \text{ mag/arcsec}^2$ correspond to badly measured galaxies (not LRGs) and have no impact in our clustering analysis.

into the mask (varying the threshold in extinction, mean error and N/pixel) does not change appreciably the measured angular correlation.

The resulting angular mask is depicted in left panel of Fig. 5 in spherical *equatorial* coordinates, with right ascension (ra) and declination (dec) along the $x - y$ axis respectively. It spans from $\sim 110^\circ$ to 260° in ra and 75° of dec almost fully in the norther hemisphere. The vertical band at $ra \sim 172^\circ$ is due to the photo- z used in this analysis (C. Cunha, private communication), that is described in the next section. Notice that we only considered the largest contiguous area of the survey, discarding stripes 76, 82 and 86 that contribute only a small fraction of the total SDSS area.

This mask covers a total area of 7136 square degrees. We have verified that this angular mask is valid in the full redshift range used in this paper, and is therefore used in all the analysis presented here.

Before moving onto the next section we include in the right panel of Fig. 5 the resulting galaxy density map in the

⁶ <http://healpix.jpl.nasa.gov>

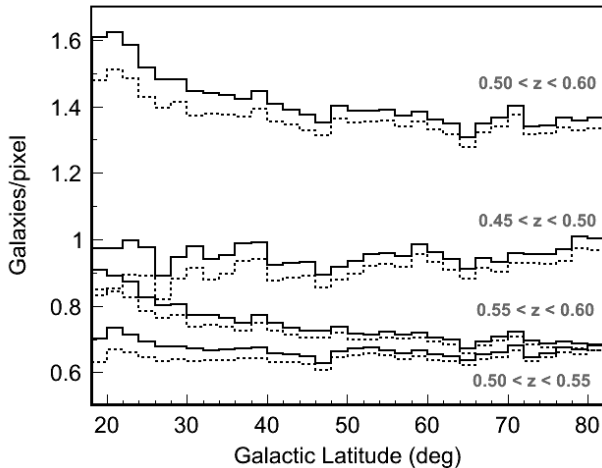


Figure 3. Histogram of number of galaxies per pixel (pixel size of 0.01 sq deg) as a function of galactic latitude for different slices in redshift as indicated in the figure. In solid line we plot the histograms when we select galaxies with $18 < mag_{50} < 24.5$, while in dashed-dot we cut $22 < mag_{50} < 24.5$. Galaxies with low mag_{50} are contaminating low galactic latitudes ($b \lesssim 25^\circ$).

same coordinates as the mask and with the same healpix pixelization ($N_{grid} = 512$). As expected, it looks homogeneous over the whole area.

2.3 Photo-z and Redshifts Distributions

In this paper we use the value added photometric catalog of Cunha et al. (2009)⁷ that is based on the Photoz2 tables of the full SDSS DR7 sample presented in Oyaizu et al. (2008).

This value added catalog was built using and extending the weighting method technique of Lima et al. (2008). As discussed in Lima et al. (2008) and Cunha et al. (2009) the technique aims at estimating the redshift distribution for a photometric galaxy sample (or selected subsamples) rather than estimating individual galaxy redshifts. Hence, as an added value the catalog provides accurate estimates of the redshift probability distribution, $p(z)$, of each galaxy.

We applied photo-z quality cuts to the catalog in order to remove badly defined $p(z)$ (e.g. double or multiple peaked distributions that can represent outliers) as well as very broad ones (that can be interpreted as galaxies with bad photo-z). To this end we impose two cuts, $|z_{peak} - z_{mean}| < 0.05$ and $\sigma_z < 0.1$, where z_{peak} is the peak of the distribution, z_{mean} is computed as $\int z p(z) dz$ and $\sigma_z = \sqrt{\int (z - z_{mean})^2 p(z) dz}$ ⁸. The first cut eliminates roughly $\sim 11\%$ of objects and the second $\sim 9\%$. Imposed together these cuts reduce the sample by $\sim 16\%$. These threshold values in σ_z and $|z_{peak} - z_{mean}|$ were obtained by identifying the tails in the distribution of values for these quantities in the full catalog. One can of course be more conservative and impose more stringent cuts but at the expense of biasing the population towards brighter objects (that typically have better photo-z) or introduce shot-noise error due

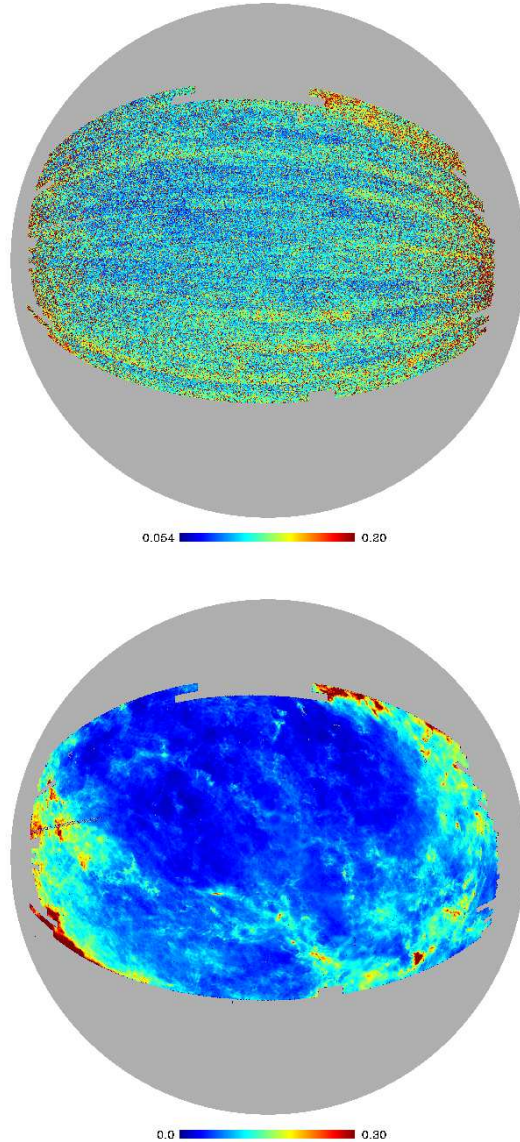


Figure 4. Top Panel shows a map of mean error in r -band magnitude per (Healpix) pixel. Bottom Panel is the distribution of galactic extinction. Noticeably the mean error is larger in zones of higher extinction (see text for details).

to large decrements in the number of galaxies per bin. Our results, in terms of the χ^2 of the best-fit models that we obtain, are robust and stable in front of the photo-z quality cut.

In this paper we split the galaxy sample into redshift bins according to whether the maximum of $p(z)$ lies in the bin or not. That is, we identify the maximum of $p(z)$ as the photometric estimate of the true redshift (z_{phot}) and do top-hat bins in photometric redshift. In turn, one of the most important ingredients in order to interpret the galaxy clustering signal is a robust estimate of the distribution in true (spectroscopic) redshift, $N(z)$, of all the galaxies in each bin. Cunha et al. (2009) discuss several methods to obtain $N(z)$ and shows, using both mock SDSS catalogs and training spectroscopic subsamples, that their best and almost

⁷ Available at http://www.sdss.org/dr7/products/value_added

⁸ The catalog provides $p(z)$ in 100 bins between $z = 0.03$ and 1.47, hence these integrals are sums over these 100 bins.

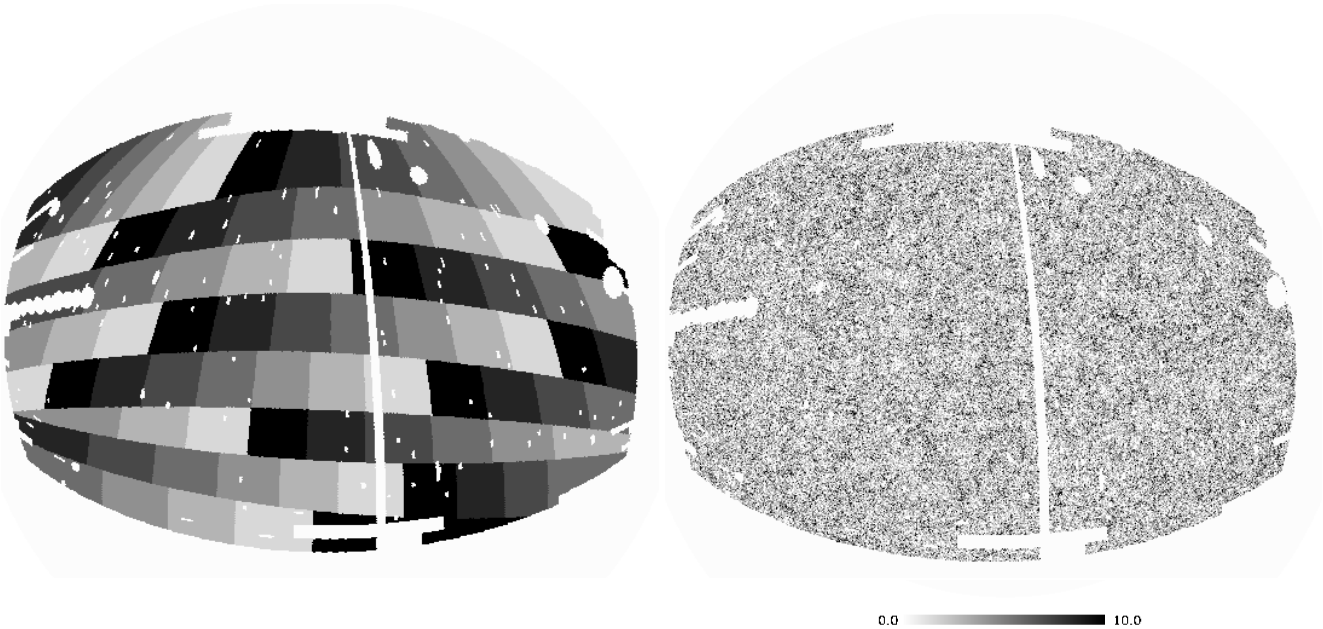


Figure 5. Left Panel: The mask used in this analysis depicted with the *Healpix* mollview projection routine. The white regions are excluded from the analysis. Different grey levels display the 81 JK zones used as one of two methods to estimate the errors. The vertical band is due to the photo- z used in this analysis. Right Panel: Angular density map of the galaxy distribution in the photometric bin $[0.5 - 0.6]$.

unbiased estimate is provided by the weighted sum of the training distribution (see also Lima et al. (2008)), which is equivalent to sum the $p(z)$ distributions of all the galaxies in the photometric bin,

$$N(z) = \sum_{i=1}^{N_{gal,bin}} p_i(z). \quad (4)$$

To test the accuracy in this determination of $N(z)$ we have selected all those galaxies in our sample that are also included in the 2SLAQ spectroscopic catalog⁹ (~ 6000 objects) and computed their distribution of true redshifts as well as $N(z)$ according to Eq. (4). These two distributions are remarkably similar as shown in Fig. 6. A Gaussian fit to each of them shows that their peak differs by less than 1% and their width by less than 9%¹⁰. This difference is in perfect agreement with the intrinsic scatter in true redshift distributions obtained from different photo- z codes (e.g. see Table A1 in Thomas et al. (2011)). Notice that we can not use 2SLAQ to estimate $N(z)$ for our complete catalog since our LRG selection is different from that in 2SLAQ (in particular the magnitude cuts). Nonetheless the previous study shows the degree of unknown in the red shift distribution. Hence we will use Eq. (4) to estimate $N(z)$ for our red shift bins and will discuss in Sec. 4.3 how our results vary when the width and/or peak change by 9% and 1% respectively.

In this way, our selected sample of LRGs have a distribution in true red shifts that peaks at $z \sim 0.5$ and extends roughly from ~ 0.4 to ~ 0.65 . For our analysis we will

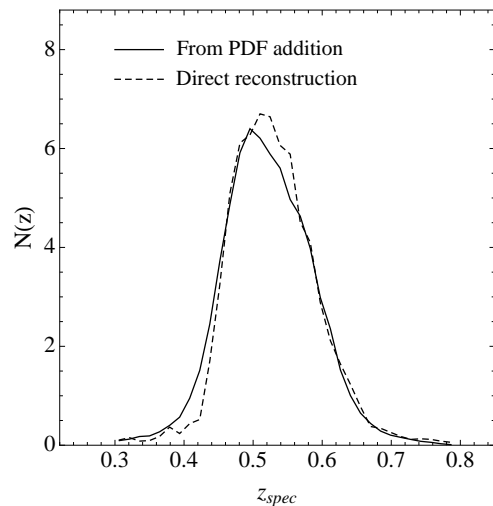


Figure 6. Direct reconstruction of the true redshift distribution for the spectroscopic sub-sample of our photometric catalog against the estimate for the same distribution using individual galaxy redshift probability distribution functions (PDF). The spectroscopic sub-sample was constructed from the 2SLAQ catalog, Cannon et al. (2006), while PDF's are provided as a part of the DR7 SDSS value added catalog of Cunha et al. (2009).

mostly refer to a single top-hat photometric redshifts bin in the range $[0.5 - 0.6]$. Figure 7 shows the true distribution of galaxies in this bin. The number of objects in this bin, after the photo- z quality cut, is 664870. Notice that the bin width is slightly larger than our typical photometric error at this redshift ($\sigma_z \sim 0.05$) hence choosing a narrower bin would

⁹ 2dF-SDSS LRG and Quasar survey, a stripe close to 0° declination within the imaging area of DR7 (Cannon et al. (2006))

¹⁰ Peak and width are defined as the mean and standard deviation of the best-fit Gaussian distribution.

yield almost the same distribution of galaxies but at the expense of increasing the noise in the measurement of $w(\theta)$ due to smaller number of particles in the bin (see below).

We also consider three narrower redshift bins, with photo- z ranges $[0.45 - 0.5]$, $[0.5 - 0.55]$ and $[0.55 - 0.6]$. The redshift distribution for these cases are shown in Fig. 8. They are clearly highly correlated and not narrower than the wider top-hat bin discussed above. The number of LRGs in these 3 bins are 451753, 317882 and 346988 respectively. In addition to an increase of shot-noise and overlap, one expects the estimation of $N(z)$ to be not so robust for a bin narrower than the intrinsic photo- z (a possible evidence for this is discussed in Sec. 4.3). These are the reasons why we decided to concentrate in a single redshift bin, and repeat our analysis in these 3 bins as consistency checks.

Redshifts bins lower than $z = 0.45$ and higher than $z = 0.6$ do not have enough number of LRGs to obtain precise measurements of the angular correlation (we find 52845 LRGs in the photometric range $[0.4 - 0.45]$ and 30412 in $[0.6 - 0.65]$). At those extreme bins our measurements also become too sensitive to our cuts (e.g. in galactic latitude and/or photo- z quality). This might be due to various reasons, for example, large magnitude errors that correlate with galactic latitude and lead to large photo- z errors.

But perhaps the most worrisome issue happens at $z > 0.6$ where we find a large extra-power over a broad range of large angular scales (already for $\theta > 1^\circ$). Excess of power¹¹ on large scales has already been found and discussed in different LRG selections based on SDSS DR5 in Sawangwit et al. (2009) and SDSS DR7 in Thomas et al. (2011, 2010) (see also Blake et al. (2007) and Padmanabhan et al. (2007)). Nonetheless, we only encounter this problem in the redshift bin $[0.6 - 0.65]$. We defer a discussion of possible reasons for Appendix A and proceed to discard these bins from our study hereafter.

3 CORRELATION FUNCTIONS

The angular correlation function measurements were performed starting from **Healpix** angular maps as described in Sec. 2.2 ($N_{\text{side}} = 512$, pixel size of $\sim 0.01 \text{ deg}^2$) and using a standard pixel estimator (Barriga & Gaztañaga (2002), Eriksen et al. (2004))

$$\hat{\omega}(\theta) = \frac{1}{N_{\text{pairs}}(\theta)} \sum_i \sum_j \delta_G^i \delta_G^j \quad (5)$$

where $\delta_G^i = N_{\text{gal}}^i / \hat{N}_{\text{gal}} - 1$ is the fluctuation in number of galaxies in the i -th pixel with respect to the mean in the angular map, pixels i and j are separated by an angle θ and $N_{\text{pairs}}(\theta)$ is the corresponding number of pixel pairs. Pixels were weighted by 0 or 1 according to the angular mask discussed in Sec. 2.2. We have also implemented a standard Landy & Szalay (Landy & Szalay 1993) estimator, and the resulting measured correlations were within 1% of that from Eq. (5).

The measured correlations in the three bins of width

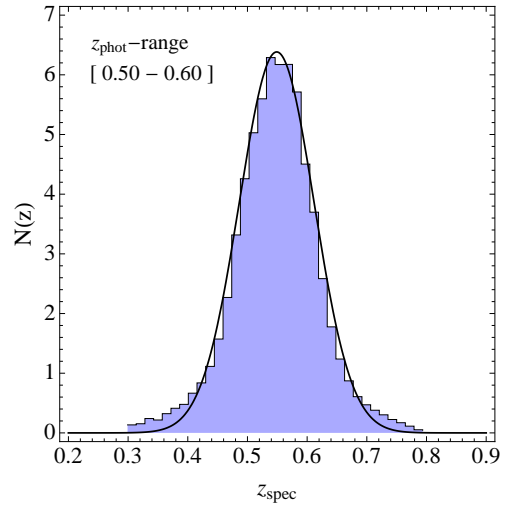


Figure 7. True (spectroscopic) redshift distribution for the bin $0.5 - 0.6$ resulting from sum of the individual redshift probability distributions. A fit to a Gaussian function (shown in solid black) yields a media of $\mu = 0.549$ and standard deviation $\sigma = 0.062$.

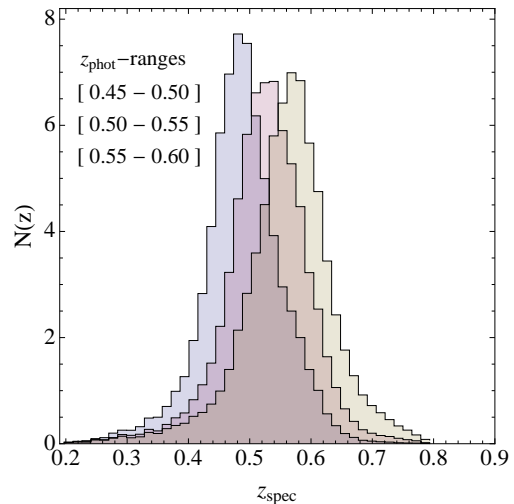


Figure 8. True redshift distribution for a set of “narrow” bins of width similar to the typical photometric error ($\Delta z = 0.05$).

0.05 as well as in the bin 0.1 are shown in Fig. 9. Error bars displayed in this figure were obtained using jack-knife resampling. In what follows we discuss our different error estimates.

3.1 Error Estimates

We estimate the error and covariance between angular bins in the measured correlation function using two independent methods.

One method was implementing the standard jack-knife resampling technique, that to date has been widely used in clustering analysis with correlation functions (for a summary see Cabré et al. (2007) and Norberg et al. (2009) and references therein). To this end we divided the angular mask in

¹¹ We note that the exact meaning of excess is only loosely defined in the literature, in general is taken a roughly more than two sigma difference between model and measurements

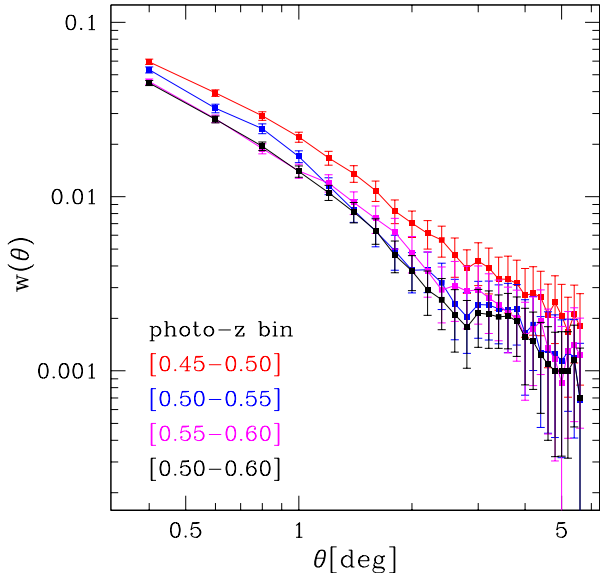


Figure 9. The measured correlation function in the different top-hat bins in photometric redshift. In this paper we focus on the bin $[0.5-0.6]$ but test the robustness of our results throughout all the redshift range.

81 jack-knife (JK) zones of similar area ($\sim 90 \text{ deg}^2$ each) and shape. These zones are shown in grey levels in Fig. 5. One then takes different realizations to be all the sampled area except from one JK zone at a time. The covariance is then computed from the dispersion among the measurements of $w(\theta)$ in the $N_{JK} = 81$ resulting realizations,

$$\text{Cov}_{JK}(\theta, \theta') = \frac{N_{JK} - 1}{N_{JK}} \sum_{i,j=1}^{N_{JK}} (w_{JK}^{(i)}(\theta) - \hat{w}(\theta)) \times (w_{JK}^{(j)}(\theta') - \hat{w}(\theta')) \quad (6)$$

where $\hat{w}(\theta)$ corresponds to the full area, $w_{JK}^{(i)}$ to the i -th realization and the factor $N_{JK} - 1$ corrects from the fact that realizations are not independent. The positive aspect of the jack-knife resampling is that this estimate is build out of the data itself and hence it can account for systematic effects difficult to capture otherwise. On the negative side is the fact that different realizations might share a large fraction of area. In principle this is accounted for by the rescaling of the covariance in Eq. (6), but this JK resampling may not reflect the true underlying statistical variance, particularly if the JK zones are too small or irregular

It is then desirable not to rely only on the jack-knife estimator. Therefore we have also calculated the error and covariance matrix using the analytical approach discussed in Crocce et al. (2011) in which,

$$\text{Cov}_{Th}(\theta, \theta') = \frac{2}{f_{sky}} \sum_{\ell \geq 0} \frac{2\ell + 1}{(4\pi)^2} P_\ell(x) P_\ell(x') (C_\ell + 1/\bar{n})^2 \quad (7)$$

where $x = \cos(\theta)$ and C_ℓ is the analytical angular power spectrum for the redshift distribution of interest. This estimate have been extensively compared against ensemble errors drawn from simulated photometric surveys assuming different binnings of the data, survey depth, underlying photo-z, shot-noise contribution and more, see Crocce et al.

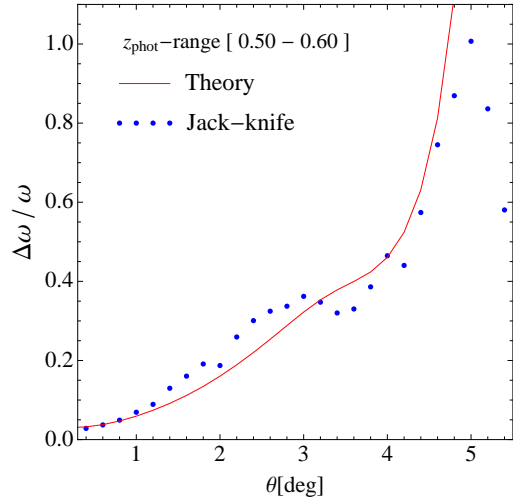


Figure 10. Relative error in the measured correlation function. Symbols correspond to Jack-knife estimates using 81 zones while solid line to the theoretical expressions in Crocce et al. (2011). In the later case the ratio is against the best-fit $w(\theta)$ model.

(2011). In turn, Ross et al. (2011) recently showed that the distribution of best-fit values for the bias and growth rate of structure recovered in survey mocks agreed very well with the errors obtained when using Eq. (7). Furthermore, these studies used an angular mask comparable to the simple geometry treated in this paper.

To compute the angular spectra in Eq. (7) we assume a Λ CDM cosmology with WMAP7 parameters (Komatsu et al. (2011)) and use the redshift distributions in Figs. 7, 8. In turn, initial values for large-scale bias b and growth rate f are obtained from a χ^2 minimization using jack-knife errors (see Sec.4). Provided with the full C_ℓ spectra we then compute the covariance matrix in Eq. (7) with $f_{sky} = 0.1682$.

Figure 10 shows the relative error $\Delta w/w$ in the measurement of the angular correlation for our main case bin in photo-z range $[0.5 - 0.6]$ (where $\Delta w \equiv \text{Cov}(\theta, \theta)^{1/2}$). The agreement with the relative error recovered from the jack-knife technique is remarkable. Figure 11 shows instead the reduced covariance matrix, $\text{Cov}_{Red}(\theta, \theta') \equiv \text{Cov}/\Delta w(\theta)\Delta w(\theta')$, obtained from the data with jack-knife (top panel) and analytically (bottom panel) They show a similar structure, with the jack-knife estimate being more noisy as expected. In addition at large angles ($\theta \gtrsim 3^\circ$) there is a stronger covariance between separated angular bins in the jack-knife estimate probably due to systematics in the data. Nonetheless, as discussed in Sec. 4, this has no major impact in our study since the recovered best-fit models (and errors) derived using either jack-knife or analytical estimates for the covariance are in broad agreement. In all, the underlying reason why the jack-knife and analytical error estimates coincide is due to the fact that the model correlation functions are in good agreement with those measured in the data. This is the subject of the forthcoming sections.

3.2 Star contamination

Lastly, we study the star contamination of the sample as a function of the redshift. The quality of the star-galaxy sep-

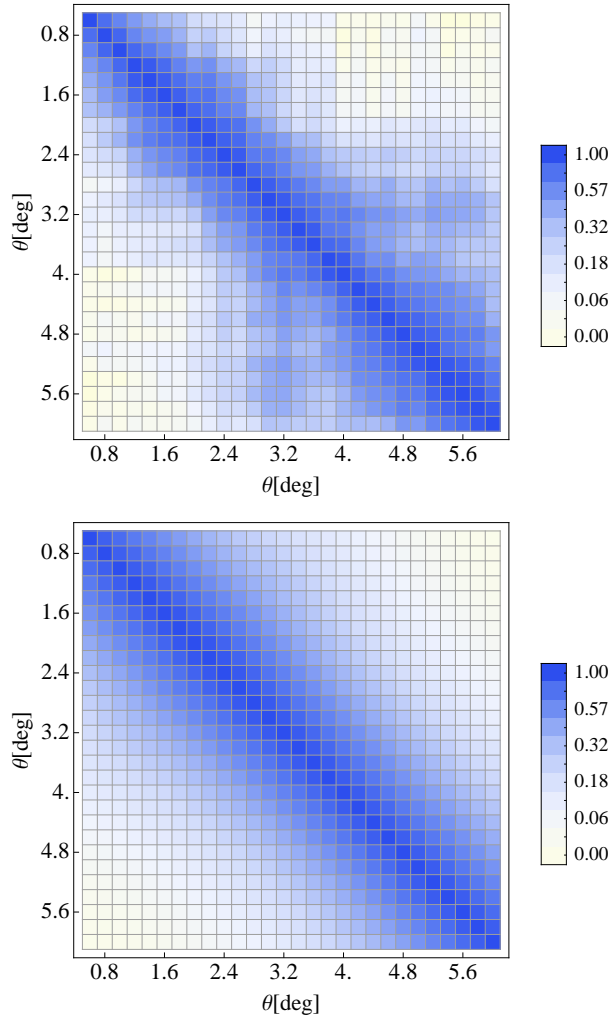


Figure 11. Reduced covariance matrix estimated with 81 Jackknife zones (top panel) or using the theoretical model in Crocce et al. (2011) (bottom panel).

aration is a major concern in photometric catalogs since the broadband colors of stars can mimic those of galaxies and yield similar photometric redshift estimates, and important distortions in the clustering signal.

We investigate the degree of contamination in our selected photometric sample performing the same selection, Eqs. (1,2,3), in the SDSS spectroscopic sample. In addition we only take the spectroscopic objects that overlap with our angular mask. For the bins where our analysis is performed we find $f_{stars} = 4 \pm 1\%$. That is, a negligible dependence with redshift and a broad agreement with the residual contamination found in comparable clustering studies at these redshifts (Sawangwit et al. (2009); Thomas et al. (2011)).

The next step is to estimate what is the impact of this contaminants in the large scale angular clustering signal since they introduce a density gradient through the galactic plane. Hence, we measure the correlation function of stars from the SDSS spectroscopic sample, relaxing the cut in *mag50* to have enough statistics. We also use the publicly available Tycho-2 star catalog (Høg et al. 2000a,b) cut to the same selection and mask as our LRG sample to obtain

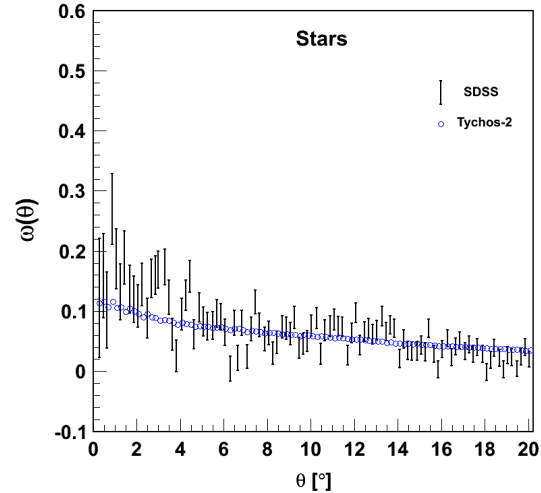


Figure 12. Angular correlation function of stars from the SDSS spectroscopic sample (error bars) and the Tycho-2 catalog (circles) verifying our sample selection and mask. The correlation is well fit by $w_{stars,fit}(\theta) = 0.0904 - 0.00313\theta$. Displayed error bars correspond to Poisson estimates, $\Delta w = (1 + w)/\sqrt{N_{pairs}}$ (negligible for Tycho-2).

a second estimate of the correlation of stars. Both determinations are in perfect agreement, as presented in Figure 12, where the lines represent the correlation function for the SDSS sample, and the circles correspond to the Tycho-2 catalog. This correlation is then included in the theoretical model for $w(\theta)$ taking into account that LRGs and stars are uncorrelated populations, as (see also Myers et al. (2006), Myers et al. (2007)):

$$w_{obs,model}(\theta, z) = (1 - f_{stars})^2 w_{gal,model}(\theta, z) + f_{stars}^2 w_{stars,fit}(\theta) \quad (8)$$

where $w_{obs,model}$ is the model for the “observed” correlation function, $w_{gal,model}$ is the model for the true correlation function of galaxies, $w_{stars,fit}$ is a simple fit to the measured correlation function for stars (see Figure 12). Notice that in Eq. (8) we have removed the explicit dependence of the star fraction and correlation with redshift for simplicity.

4 BIAS AND GROWTH OF STRUCTURE

In this section we will employ the measured angular correlation function to place joint constraints in the growth rate of structure and bias of the LRG sample.

4.1 Theoretical model

We will use the theoretical model for the angular correlation function presented in Crocce et al. (2011). It was extensively tested against mock catalogs of photometric surveys with specifications similar to our present case. It was shown that the inclusion of redshift-space distortions and bias to linear order together with a model for non-linear matter clustering accurately reproduced the measured angular correlation in scales $\theta \gtrsim 0.5^\circ$ for redshift bins centered at $z \sim 0.5$. We

now recall some basic expressions of the model and refer the reader to Crocce et al. (2011) for further details.

The model angular correlation function is given by,

$$w_{gal,model}(\theta) = \int dz_1 n(z_1) \int dz_2 n(z_2) \xi^s(\mathbf{r}_{12}) \quad (9)$$

where $\mathbf{r}_{12} = \mathbf{r}_{12}(z_1, z_2, \theta)$ is the separation of a pair of galaxies at redshift z_1 and z_2 subtending an angle θ with the observer. In turn, $n(z)$ is the spectroscopic redshift distribution of the photometric sample under study. Notice that the inclusion of photo- z errors in the theory is solely through $n(z)$ (e.g. Budavári et al. (2003)).

Given the area and mean redshift of our sample we are allowed to make the plane-parallel approximation (see Racanelli et al. (2010) and references therein for discussions of its validity). In this limit, the redshift space correlation is given by (Hamilton (1992))

$$\xi^s(s, \mu) = \xi_0(s)P_0(\mu) + \xi_2(s)P_2(\mu) + \xi_4(s)P_4(\mu) \quad (10)$$

where P_ℓ denote the standard Legendre polynomials, $s^2 = r^2(z_1) + r^2(z_2) - 2r(z_1)r(z_2)\cos\theta$ and $\mu = (r(z_2) - r(z_1))/s$, with $r(z)$ being the comoving distance to redshift z . The ξ_ℓ are the multi-poles of the spatial correlation

$$\begin{aligned} \xi_0(r) &= (b^2 + 2bf/3 + f^2/5) [\xi(r)] \\ \xi_2(r) &= (4bf/3 + 4f^2/7) [\xi(r) - \xi'(r)] \\ \xi_4(r) &= (8f^2/35) [\xi(r) + 5/2 \xi'(r) - 7/2 \xi''(r)] \end{aligned} \quad (11)$$

with $\xi' \equiv 3r^{-3} \int_0^r \xi(x)x^2 dx$ and $\xi'' \equiv 5r^{-5} \int_0^r \xi(x)x^4 dx$. Hence the angular correlation in Eq. (9) can be written as,

$$w(\theta) = (b^2 + 2bf/3 + f^2/5) w_0(\theta) + (4bf/3 + 4f^2/7) w_2(\theta) + (8f^2/35) w_4(\theta) \quad (12)$$

where $w_\ell(\theta)$ are the bin projection of the functions in square brackets in Eq. (11). Equation (12) can of course be rearranged into three terms scaling as b^2 , bf and f^2 ,

$$w(\theta) = b^2 w_0(\theta) + bf (2/3 w_0(\theta) + 4/3 w_2(\theta)) + f^2 (1/5 w_0(\theta) + 4/7 w_2(\theta) + 8/35 w_4(\theta)). \quad (13)$$

The fact that each of these 3 terms have a different angular dependence (through the different linear combinations of w_ℓ) makes it possible to constrain both b and f at the same time. These terms are displayed in Fig. 13 (without the multiplicative factors involving b and f). The BAO is only present in the $\ell = 0$ or “real-space” term determined by the bias. In real space the correlation becomes negative for scales larger than $\sim 4^\circ - 5^\circ$. The effect of RSD, in particular of the cross term bf , is to make the correlation positive until larger scales, broadening the BAO feature (see also Fig. 5 in Crocce et al. (2011)). Hence, at these scales the value of f can be degenerate with “excess-power” caused by systematic effects that also make the correlation positive (e.g. extinction, star-galaxy separation or magnitude errors).

4.2 Fits to growth and bias

We will now use the measurements of the angular correlation function and the model described above to investigate the constraining power of the SDSS LRG photometric catalog onto the two-parameter space given by the velocity growth factor f and large-scale galaxy bias b . Recall however that

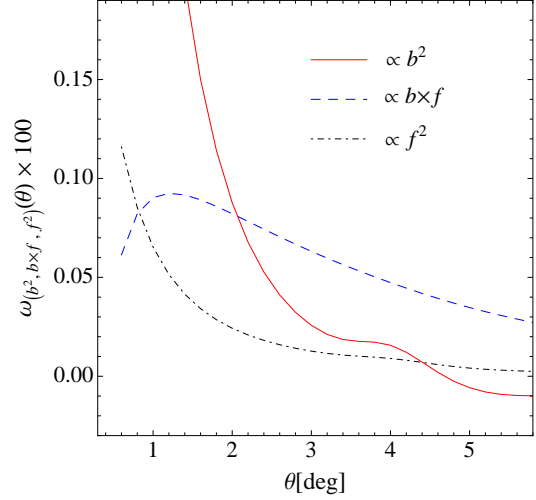


Figure 13. Angular dependence of the three additive terms making up the model angular correlation. They are proportional to $b^2(z)$, $b(z)f(z)$ and $f^2(z)$ (in units of $\sigma_8(z)$) and are shown in solid red, dashed blue and dot-dashed black respectively. Their different shapes make it possible to constrain simultaneously $b(z)$ and $f(z)$. This figure corresponds to our photo- z bin $[0.5 - 0.6]$.

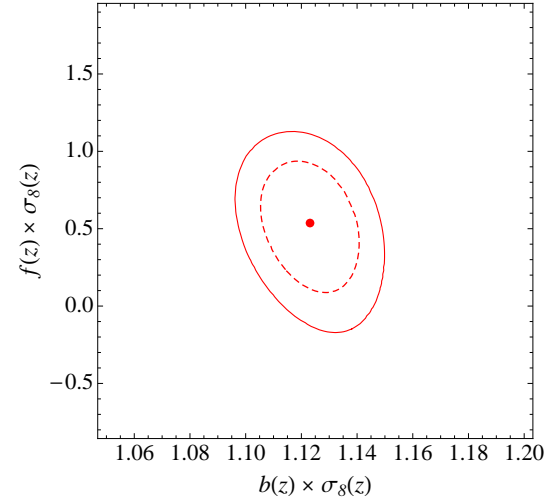


Figure 14. Two dimensional constraints in $f \times \sigma_8(z)$ and $b(z) \times \sigma_8(z)$. Dashed line corresponds to the $1 - \sigma$ marginalized contour ($\Delta\chi^2 = 1$) and solid line to the unmarginalized case ($\Delta\chi^2 = 2.3$). In our fiducial cosmology $\sigma_8(z = 0.5) = 0.61$, leading to best-fit values $f(z = 0.5) = 0.87$ and $b(z = 0.5) = 1.84$

the multipoles ξ_ℓ are arbitrarily normalized to, say, the amplitude of fluctuations $\sigma_8(z = 0)$ in spheres of $8h^{-1}$ Mpc (e.g. Song & Percival (2009)). Thus, f and b are perfectly degenerate with this normalization and our two parameter space is in fact given by $b(z)\sigma_8(z)$ and $f(z)\sigma_8(z)$, where $\sigma_8(z) = D(z)\sigma_8(z = 0)$ and $D(z)$ is the linear growth factor.

Notice that we will not make any assumption for the relationship between the velocity growth factor f and cosmological parameters, but rather take f as a free-parameter. In particular we will not assume that the underlying theory

redshift bin	$b(z)\sigma_8(z)$	$f(z)\sigma_8(z)$	dD/da
0.15 – 0.30	1.46 ± 0.16	0.49 ± 0.10	0.76 ± 0.15
0.30 – 0.40	1.28 ± 0.08	0.42 ± 0.06	0.70 ± 0.10
0.40 – 0.47	1.46 ± 0.16	0.50 ± 0.12	0.90 ± 0.21
0.50 – 0.60	1.12 ± 0.02	0.53 ± 0.42	1.04 ± 0.81

Table 1. Best-fit values for bias, velocity growth factor and growth rate. Top three rows correspond to the analysis of spectroscopic SDSS LRG data as presented in Cabré & Gaztañaga (2009). Bottom row to our single redshift bin using the photometric LRG catalog.

of gravity is General Relativity (where to a good approximation $f = \Omega_m^\gamma(z)$ and $\gamma = 0.55$) because our ultimate goal is in fact understanding to what extent photometric data can help to constrain GR.

This is different from other works in the literature where constraints from redshift space distortions for f (or $\beta = f/b$) are recast or combined with the ones for Ω_m assuming GR (e.g. Padmanabhan et al. (2007), Blake et al. (2007), Thomas et al. (2011), see also Sec. 4.4). Our approach corresponds to the *free growth* model of Samushia et al. (2011).

For the cosmological model we will assume a Λ CDM universe compatible with WMAP7 (Komatsu et al. (2011)) with $\Omega_m = 0.272$, $\Omega_{DE} = 0.728$, $\Omega_b = 0.0456$, $n_s = 0.963$, $h = 0.704$. In our approach these parameters determine the shape of the real-space matter correlation function and the distance-redshift relation.

As shown in Sec. 2.3 splitting the data in multiple bins results in samples that are highly correlated. Thus, we decided to focus in a single redshift bin to present our main results and defer the study of narrow bins to Sec. 4.3, in the context of robustness and consistency studies.

Hence we concentrate on the bin $[0.5 - 0.6]$. This width is about twice the typical photometric error while the center of the bin makes this data uncorrelated with the SDSS LRG spectroscopic sample (that we refer to later on). The estimate for the true redshift distribution of galaxies in this bin is shown in Fig. 7. Using a spline-fit to it we computed the observed model correlation following Eqs. (8,9-12) sampling the two-parameter space given by $f\sigma_8 - b\sigma_8$. We then performed a standard χ^2 minimization, where

$$\chi^2(f\sigma_8, b\sigma_8) = \sum_{i,j=1}^{N_{bin}} \Delta w(\theta_i) \text{Cov}_{ij}^{-1} \Delta w(\theta_j) \quad (14)$$

and $\Delta w \equiv w_{obs,model}(f\sigma_8, b\sigma_8) - w_{measured}$. To begin with we use the jack-knife covariance. The resulting best-fit values and $1 - \sigma$ errors are listed in Table 1 (to convert to f and b one can use that $\sigma_8(0.55) = 0.611$ for our fiducial cosmology if $\sigma_8(z=0) = 0.8$). The fit yields $\chi^2_{min} = 26.67$ for 28 bins in θ in the range $[0.6^\circ - 6^\circ]$ and two fitting parameters. Hence the quality of the fit is very good. The joint error distribution is displayed in Fig. 14 and shows that these two parameters are not degenerate. The significance of RSD in our data is $\sim 1.26\sigma$ (i.e. the degree by which the recovered value for f is away from zero).

Alternatively one can assume that the velocity growth rate is given by General Relativity, i.e. $f(z)\sigma_8(z) =$

$\sigma_8(z)d \ln D(z)/d \ln a = 0.45$ (for our fiducial cosmology and $\sigma_8(z=0) = 0.8$), and fit only for the overall amplitude of clustering. In this case we recover a similar $\chi^2_{min} (= 26.7)$ and $b\sigma_8 = 1.125 \pm 0.017$. Hence the fit does not vary appreciable, showing that agreement with standard Λ CDM is also very good and that the sensitivity of our data to redshift-distortions is weak, as expected.

The results so far were obtained assuming 4% star contamination (as discussed in Sec. 3.2 and Eq. (8)). If we now assume that our sample is perfectly clean of stars ($f_{stars} = 0$) we get $b\sigma_8 = 1.08 \pm 0.02$ and $f\sigma_8 = 0.66 \pm 0.39$ and a $\chi^2_{min} = 26.87$. This model is hardly differentiable from the case with $f_{stars} = 4\%$ (the χ^2 becomes only negligible worse), see Fig. 15. Hence stellar contamination can mimic the effect of RSD and become a worrisome source of systematic effect in future and better data. In the present case the agreement between the best-fit value of f and the “GR” value degrades only slightly when $f_{star} = 0$, with differences well within the errors. We conclude that the star contamination in our sample is sufficiently under control and does not drive our results.

Figure 15 shows the resulting best-fit models discussed above against the measured angular correlation function. In all cases the model matches the data quite well in all the angular range, with no signal of excess-clustering on large scales. This is to some extent at variance with the recent study by Thomas et al. (2011) (see also the follow up Thomas et al. (2010)) who finds the amplitude of the angular power spectra of photometric LRGs to have a $2-\sigma$ excess clustering away from the Λ CDM prediction at the lowest multipoles. This result was obtained using the MegaZ catalog over three redshift bins in the range $[0.4-0.65]$. The MegaZ catalog is also build upon the DR7 SDSS photometric catalog. However the LRG selection criteria in MegaZ is different from the one in this paper, most notably by the magnitude cuts ($i_{dev} < 19.8$ in MegaZ compared to $petror < 21$ in our case)¹² but also in the color and mag_{50} cuts intended to isolate stars from galaxies. The photo-z code used for MegaZ is also different from ours, although both are based in the ANNz code of Collister & Lahav (2004). Sawangwit et al. (2009) also finds an excess clustering when searching for the baryon acoustic scale, but this result is difficult to compare with ours as they use an over simplified method to stack the signal from wider redshift bins calibrated with different spectroscopic samples.

The constraints recovered so far, albeit large, match the study of Ross et al. (2011) that forecast how well redshift distortions can potentially be measured with galaxies selected from a photometric survey. This match can be clearly seen from their Fig. 8 after scaling the results for a sample of unbiased galaxies binned around $z = 0.5$ by our bias factor $b \sim 2$ (since $\Delta(f\sigma_8) \propto b$). For our redshift bin width the forecast yields $\Delta(f\sigma_8) \sim 0.4 - 0.5$, in very good agreement with the results we obtain with the actual data (e.g. see Table 1). This implies that systematics, photo-z errors,

¹² The MegaZ selection is done to match the magnitude cut in 2SLAQ from where the photo-z calibration is obtained. We find that the angular correlation of galaxies in MegaZ matches the clustering amplitude in our sample if we cut in $petror < 20.7$. Hence MegaZ is slightly brighter than our sample.

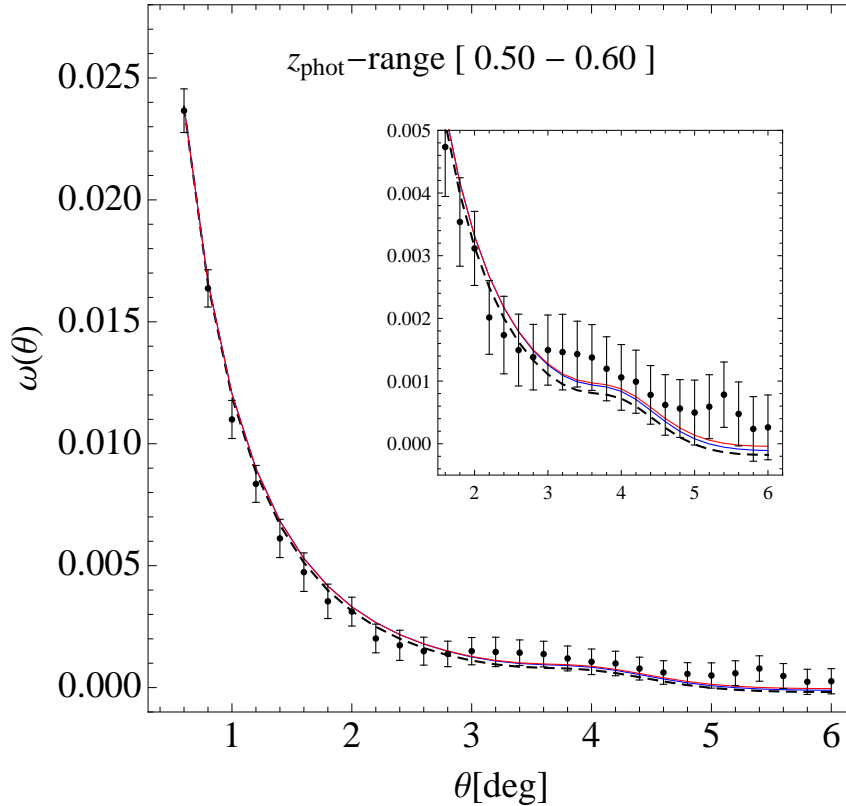


Figure 15. Angular correlation function in our central bin of width 0.1 centered at $z = 0.55$. Solid red line is our best-fit model including the effect of star contamination ($f_{star} = 4\%$). Solid blue line is the corresponding best-fit model if $f_{star} = 0$. The values for f and b are given in Table 1. For reference we include with a dashed black line a WMAP7 Λ CDM model assuming General Relativity, that is with f set to $\Omega_m^{0.55}$ ($f_{star} = 0$ in this case). The inset panel zooms in the region where the baryon acoustic peak is located (see Fig. 18 for the BAO significance). Notably the different models match the data very well in all the range of scales.

selection and modeling can be controlled sufficiently well in present photometric data to yield expected constraints of redshift distortions. Near future data, provided with a better handle on systematics due to stars and photo- z , should be able to complement shallower spectroscopic surveys in placing bounds to the growth of structure in the universe.

4.3 Robustness and impact of systematics effects

In this section we investigate different components of our analysis that could potentially change our results.

Analytical Covariance Matrix: We now investigate how our results change when we use the analytical error estimate discussed in Sec. (3.1). This estimate accounts for statistical and shot-noise errors but does not account for systematic errors introduced by, say, stars (at least in the way presented in Crocce et al. (2011)). Hence we compute the C_ℓ spectra, and Cov_{Th} , in Eq. (7) using the best-fit values for f and b corresponding to the model with $f_{stars} = 0$ discussed above. Using this covariance the best-fit values to the angular correlation in the bin $[0.5 - 0.6]$ change to $b\sigma_8 = 1.13 \pm 0.02$ and $f\sigma_8 = 0.35 \pm 0.54$ while the χ^2_{min} degrades to 32 (for a model with $f_{stars} = 4\%$). Hence the change in the recovered best-fit values is within half σ compared to the results shown

in Table 1. In turn, the error in $b\sigma_8$ is unchanged while that in $f\sigma_8$ increases by about 25%.

The resulting model matches the data as well as the one derived using jack-knife errors and the goodness of the fit are comparable. The only difference is in the resulting error on the velocity growth factor. This may be due to the structure of the covariance on large separations that may be affected by some systematics not captured by the theoretical estimate.

Redshift Distribution: One important but difficult to estimate component in clustering analysis of photometric data is the distribution of galaxies in true redshift. In Sec. 2.3 we studied the degree of uncertainty left in the estimate of $N(z)$, about 1% in the peak position and 9% in the width. To investigate the impact of this systematic in our analysis we computed the model correlation and found best-fit parameters assuming $N(z)$ is a Gaussian distribution with $\mu = 0.549$ and $\sigma_z = 0.062$ (model-1), that are the best-fit values to $N(z)$ in Fig. 7. We then recomputed the model by increasing μ by 1% and decreasing σ_z by 9% (model-2), and subsequently did the best-fit analysis. The χ^2 of these two models is almost equal, changing by $\sim 1\%$. The resulting best-fit values for $b\sigma_8$ decrease from 1.12 ± 0.02 (for model-1) to 1.08 ± 0.02 (for model-2) while from 0.76 ± 0.57 to 0.7 ± 0.5 for $f\sigma_8$. This is because a narrower $N(z)$

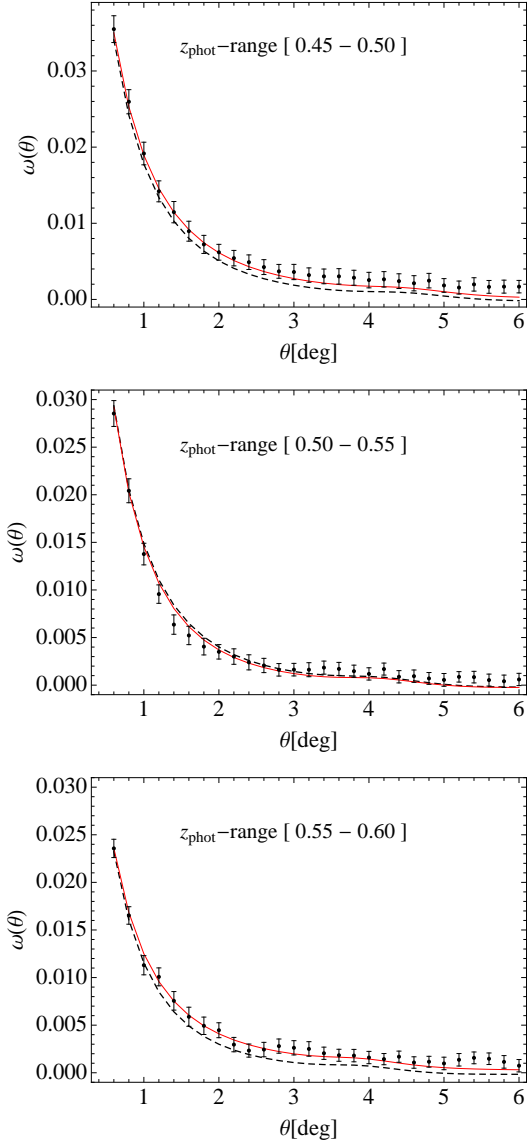


Figure 16. Angular correlation function in “narrow” bins of width comparable to the underlying photometric error, as indicated in the panels. Solid red lines are the best-fit models taking into account the $\sim 4\%$ star contamination in our sample. Dashed line correspond to a standard Λ CDM model with $f_{star} = 0$ and growth given by General Relativity, i.e. $f(z) = \Omega_m(z)^{0.55}$.

implies less bin projection what leads to a higher amplitude angular correlation and slightly more sensitivity to redshift distortions (Nock et al. (2010); Crocce et al. (2011)). These differences are only marginal given the overall large errors provided by present photometric data. However future surveys will probably need more accurate estimates of $N(z)$.

Narrower redshift bins: As mentioned earlier we have also considered splitting the data into 3 narrower bins of width similar to the typical photo- z error : $[0.45 - 0.5]$, $[0.50 - 0.55]$ and $[0.55 - 0.60]$. The galaxy redshift distributions for these bins are shown in Fig. 8 while the measured correlations and best-fit models are displayed in Fig. 16.

The best-fit values for the bias in each bin decreases

slightly with increasing redshift: $b\sigma_8 = 1.26, 1.21$ and 1.1 respectively (with 2% error).

In turn the best-fit values for $f\sigma_8$ are 1.14 ± 0.57 , 0.024 ± 0.53 and 1.39 ± 0.46 respectively (assuming $f_{star} = 4\%$). Hence we see some spread in the recovered values for the velocity growth rate. Compared to the corresponding values in GR they still agree at $\sim 1 - 2\sigma$.

As discussed before a bin width smaller or comparable to the photo- z is subject to large bin to bin migration (in other words, the estimate of $N(z)$ itself is more sensitive to photo- z unknowns). Therefore we expect to recover more robust results in bins larger than the underlying photo- z .

4.4 Implications for the growth rate and comparison with spectroscopic studies

We now put our results in context of similar ones derived using spectroscopic data. In Table 1 we show constraints in $b(z)\sigma_8(z)$ and $f(z)D(z)$ as obtained by Cabré & Gaztañaga (2009) using spectroscopic LRGs from SDSS. Table 2 in Cabré & Gaztañaga (2009) list the best fit values of the clustering amplitude $Amp \equiv b(z)\sigma_8$ and Ω_m . This Table refers to σ_8 at $z = 0$ because the best fit value of Ω_m was used to estimate the linear growth $D(z)$ at the corresponding redshift according to standard cosmological equations in General Relativity (GR). Here we do not want to assume GR or any other relation between Ω_m and $D(z)$ and we therefore scale these amplitudes back to the original data amplitudes, i.e. $\sigma_8(z)$, by multiplying Amp by the best fit value of $D(z)$ in GR. The resulting amplitudes are listed here as $b(z)\sigma_8(z)$ in Table 1. We can then find an estimate of $f(z)\sigma_8(z)$ by just multiplying these $b(z)\sigma_8(z)$ estimates with the values of β listed in Table 1 of Cabré & Gaztañaga (2009) for the corresponding samples.

One can turn these values, and those at $z = 0.55$ from the photometric data, into estimates for the linear growth rate of structure as follows,

$$\frac{\partial D}{\partial a} = \frac{D(z)}{a} f(z) = \frac{1+z}{\sigma_8(0)} f(z)\sigma_8(z), \quad (15)$$

where we assume our fiducial value $\sigma_8(0) = 0.8$ (consistent with, e.g., Tinker et al. (2011)). Results are listed in Table 1 and displayed altogether in Fig. 17. Provided with them one give constraints in the growth index assuming the γ -parameterization of the growth, for which $f = \Omega_m(z)^\gamma$ and γ is a scale and redshift independent constant, Linder (2005). In this case,

$$\frac{\partial D}{\partial a} = (1+z)D(z)\Omega_m(z)^\gamma \quad (16)$$

and $D(z) = \exp(-\int_0^z \Omega_m(x)^\gamma / (1+x) dx)$. This yields

$$\gamma = 0.54 \pm 0.17 \quad (17)$$

for the combination of spectroscopic and photometric data given in the fourth column of Table 1.

Before moving on we note that novel constraints on the growth rate up to $z = 0.9$ were very recently reported by the WiggleZ survey using blue galaxies instead of LRGs (Blake et al. (2011)). At $z < 0.5$ they improve to some extent over the ones we used, e.g. $\Delta(f\sigma_8) = 0.07$ at $z = 0.2$ and $\Delta(f\sigma_8) = 0.04$ at $z = 0.4$ (see Table 1). At $z > 0.5$ they

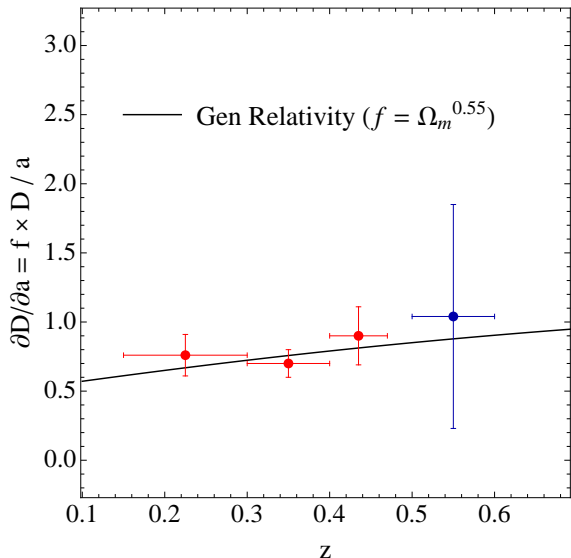


Figure 17. Linear growth rate of structure from LRG spectroscopic data in the range $[0.15-0.47]$, as presented in Cabré & Gaztañaga (2009), and from our analysis of photometric data at $z = 0.55$ (assuming $\sigma_8(0) = 0.8$). These data leads to $\gamma = 0.54 \pm 0.17$ in a model where $f = \Omega_m(z)^\gamma$.

are considerably tighter than those we derive with imaging data, as expected. Yet, for concreteness we have decided to present our results in terms of SDSS LRG clustering (either spectroscopic or photometric) as the focus of the paper is to demonstrate that imaging data is able to yield constraints in RSD.

5 BARYON ACOUSTIC OSCILLATIONS

One of the most important probes of the accelerated cosmic expansion is the existence of an excess clustering imprinted at a well defined comoving length scale of about $\sim 100 h^{-1} \text{Mpc}$ in the correlation of galaxies and $\sim 1^\circ$ in the one of CMB photons. It originates in the coupling of the baryon-photon plasma prior to recombination and hence can be very well determined with CMB data. Provided with this estimate it can then be measured with galaxy data and used to constrain the distance-redshift relation in the local universe, that in turn is sensitive to the nature of dark-energy (and/or the appropriate law of gravity). The main obstacle of this pathway is that the excess clustering signal in galaxies represents only $\sim 1\%$ over that of a random distribution. Nonetheless several surveys are dedicated or include BAO in their scientific plans.

The BAO signature have been extensively studied in the clustering of spectroscopic data, in particular using LRGs since they span the largest volume possible compared to other galaxy types (e.g. Eisenstein et al. (2005); Hütsi (2006); Percival et al. (2007); Gaztañaga et al. (2009); Cabré & Gaztañaga (2009); Gaztañaga et al. (2009); Kazin et al. (2010); Percival et al. (2010)). The advantage in this case is that one has three dimensional information to sample this 1% excess of pairs. The disadvantage is that the sampling of the over-density field is much more poorer with spectra and

is eventually limited to lower redshifts when compared to photometric catalogs (which on the converse only yield projected quantities with lower significance). Hence it is very important to investigate what evidence for this signature is already present in our data given the number of such photometric surveys already undergoing or planned for the near-future.

The use of photometric data to investigate BAO has been relegated to some extent, probably due to the lower signal-to-noise, the impact of systematics and the quality of the photo- z . In Blake et al. (2007) and Padmanabhan et al. (2007) this signature was studied stacking photometric redshift bins in order to reconstruct the 3D spectrum. Both studies find evidence for BAO at $< 3\sigma$. In turn, only Sawangwit et al. (2009) (to our knowledge) have explored the possibility of locating the signature in configuration space, with ambiguous results (e.g. too high in amplitude compared to ΛCDM expectations).

We will now investigate how well our measurements agree with the shape of the model correlation including or excluding the effect of baryons. In a separate paper we present a detailed analysis of the significance and implication of the baryon acoustic peak imprinted in the angular clustering of our sample, see Carnero et al. (2011).

Figure 18 shows the measured angular correlation in the photo- z bin $[0.5 - 0.6]$ in a way that highlights the shape of $w(\theta)$ at large angular scales. We also display the standard Eisenstein & Hu (1998) model prediction including the baryons effect (solid blue) and excluding it, i.e. with the wiggles smoothed out (solid red). Figure 18 shows a quite clear bump in the correlation function at $\theta \sim 4^\circ$, in very good agreement with the model in both shape and location. For this figure we have not attempted to fit for redshift distortion parameter $f(z)$ as in Sec. 4.2 but rather have assumed GR ($f(z = 0.55) = 0.74$) and fit for the overall bias only (with fixed cosmological parameters as given in Sec. 4.2). We note that the “BAO” model correlation obtained with the approximation of Eisenstein & Hu (1998) is very similar the one derived with CAMB in Sec. 4.2.

To estimate the statistical significance of this feature we compare the two best-fit models, with and without BAO. The difference in their χ^2 yields 5.4 suggesting that the BAO model is preferred with a significance $\sim 2.3\sigma$ ($\sim 98\%$ confidence). Notice that both models have the same number of degrees of freedom since only the bias is fit. This result is un-changed if we allow for 4% star contamination in both models and is in perfect agreement with the finding of Carnero et al. (2011) using a completely independent analysis method.

Although the significance is low the good agreement with ΛCDM expectations is very encouraging for future photometric campaign that will achieve better error bars thanks to improved photo- z and survey depth. In addition this is, to our knowledge, the first time the BAO bump is clearly depicted in agreement with ΛCDM predictions in the angular correlation of photometric LRG data at this high redshift.

6 CONCLUSIONS

In this paper we used the angular correlation function of the imaging sample of luminous red galaxies in the DR7

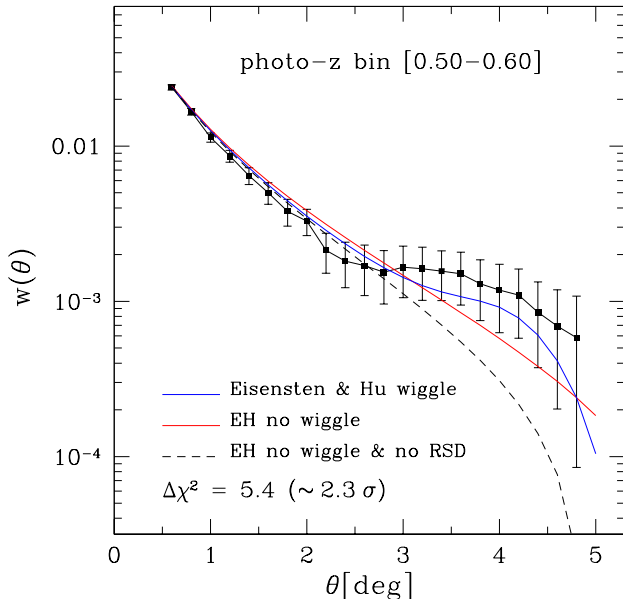


Figure 18. *Baryon Acoustic Feature at $z = 0.55$.* The plot shows the Eisenstein & Hu (1998) model with and without baryons. The data and model agree quite well in both amplitude and shape of the acoustic bump. The BAO feature is detected here with a 98% confidence level (2.3σ significance). Dashed line corresponds to the no-wiggle model when RSD are ignored. This shows the importance of both BAO and RSD to account for observations.

of the SDSS as a testing ground for measuring the growth rate of expansion through redshift space distortions using photometric data. In addition we investigated the evidence for the baryon acoustic feature in the angular correlation.

We put a strong emphasis in the selection of the galaxy sample and overall robustness against several systematic effects, such as magnitude errors, bad extinction zones, photo-z outliers and more. We paid particular attention to the impact of stellar contamination in the angular clustering measurements. On the one hand we minimized such contamination introducing a cut in surface brightness, mag_{50} . On the other we estimated the distortion that the residual contamination introduces in the correlation measurements.

Our measured correlation, in the range $[0.50 - 0.60]$ is in good agreement with expectations from standard Λ CDM. In particular it shows no excess clustering on the largest scales, contrary to other works in the literature. This is an encouraging proof that systematic effects in photometric data can be controlled sufficiently well to use them as a cosmological tool (Blake et al. (2007); Padmanabhan et al. (2007); Thomas et al. (2011)). The distortions introduced by the intrinsic clustering of contaminating stars does not change our results but might become a worrisome source of systematic biases in future surveys with smaller error bars. A similar conclusion was reached in regards to the estimation of the true redshift distribution of the sample.

Indeed, we found that redshift space distortions can be measured using photometric data, albeit with large error bars due to the high-bias of the sample and the poor photo-z error. Our results are in very good agreement with the recent forecast by Ross et al. (2011). Hence, this paper can

be taken as a validation of the forecast for a SDSS like-case as presented in Ross et al. (2011) and a proof-of-concept of the promising expectations for upcoming photo-z surveys such as DES, Euclid and PannStars.

In addition we found quite a strong evidence for the baryon acoustic peak in the measured angular correlation, something not observed before. The shape, amplitude and location of the BAO feature is in very good agreement with Λ CDM expectations yielding a $\sim 2.3\sigma$ significance over a model without BAO. In a separate work, Carnero et al. (2011), we discuss this detection of BAO and its cosmological implication using an independent analysis from the one presented here.

In all, our results strengthen the expectations on the ability of future photometric surveys to compete and/or complement spectroscopic data, as well as to serve to other approaches such as weak lensing or supernovae, in the quest to understand the nature of cosmic acceleration.

ACKNOWLEDGEMENTS

We are thankful to Carlos Cunha for his help with photo-z. Funding for the SDSS and SDSS-II has been provided by the Alfred P. Sloan Foundation, the Participating Institutions, the National Science Foundation, the U.S. Department of Energy, the National Aeronautics and Space Administration, the Japanese Monbukagakusho, the Max Planck Society, and the Higher Education Funding Council for England. The SDSS Web Site is <http://www.sdss.org/>.

The SDSS is managed by the Astrophysical Research Consortium for the Participating Institutions. The Participating Institutions are the American Museum of Natural History, Astrophysical Institute Potsdam, University of Basel, University of Cambridge, Case Western Reserve University, University of Chicago, Drexel University, Fermilab, the Institute for Advanced Study, the Japan Participation Group, Johns Hopkins University, the Joint Institute for Nuclear Astrophysics, the Kavli Institute for Particle Astrophysics and Cosmology, the Korean Scientist Group, the Chinese Academy of Sciences (LAMOST), Los Alamos National Laboratory, the Max-Planck-Institute for Astronomy (MPIA), the Max-Planck-Institute for Astrophysics (MPA), New Mexico State University, Ohio State University, University of Pittsburgh, University of Portsmouth, Princeton University, the United States Naval Observatory, and the University of Washington.

We thank the Spanish Ministry of Science and Innovation (MICINN) for funding support through grants AYA2009-13936-C06-01, AYA2009-13936-C06-03, AYA2009-13936-C06-04 and through the Consolider Ingenio-2010 program, under project CSD2007-00060.

REFERENCES

- Abazajian K. N., Adelman-McCarthy J. K., Agüeros M. A., Allam S. S., Allende Prieto C., An D., Anderson K. S. J., Anderson S. F., Annis J., Bahcall N. A., et al. 2009, *ApJS*, 182, 543
- Barriga J., Gaztañaga E., 2002, *MNRAS*, 333, 443
- Blake C., Bridle S., 2005, *MNRAS*, 363, 1329

Blake C., Collister A., Bridle S., Lahav O., 2007, MNRAS, 374, 1527

Blake C., et al., 2011, MNRAS, pp 834–+

Budavári T., et al., 2003, ApJ, 595, 59

Cabré A., Fosalba P., Gaztañaga E., Manera M., 2007, MNRAS, 381, 1347

Cabré A., Gaztañaga E., 2009, MNRAS, 393, 1183

Cabré A., Gaztañaga E., Manera M., Fosalba P., Castander F., 2006, MNRAS, 372, L23

Cannon R., et al., 2006, MNRAS, 372, 425

Carnero A., Sánchez E., Crocce M., Cabré A., Gaztañaga E., 2011, ArXiv e-prints

Colless M., et al., 2001, MNRAS, 328, 1039

Collister A. A., Lahav O., 2004, PASP, 116, 345

Crocce M., Cabré A., Gaztañaga E., 2011, MNRAS, pp 385–+

Cunha C. E., Lima M., Oyaizu H., Frieman J., Lin H., 2009, MNRAS, 396, 2379

Drinkwater M. J., et al., 2010, MNRAS, 401, 1429

Eisenstein D. J., et al., 2001, AJ, 122, 2267

Eisenstein D. J., et al., 2005, ApJ, 633, 560

Eisenstein D. J., Hu W., 1998, apj, 496, 605

Eriksen H. K., Lilje P. B., Banday A. J., Górski K. M., 2004, ApJS, 151, 1

Gaztañaga E., Cabré A., Castander F., Crocce M., Fosalba P., 2009, MNRAS, 399, 801

Gaztañaga E., Cabré A., Hui L., 2009, MNRAS, 399, 1663

Górski K. M., Hivon E., Banday A. J., Wandelt B. D., Hansen F. K., Reinecke M., Bartelmann M., 2005, ApJ, 622, 759

Hamilton A. J. S., 1992, ApJL, 385, L5

Høg E., et al., 2000a, A&A, 363, 385

Høg E., et al., 2000b, A&A, 355, L27

Hütsi G., 2006, A&A, 449, 891

Kazin E. A., et al., 2010, ApJ, 710, 1444

Komatsu E., et al., 2011, ApJS, 192, 18

Landy S. D., Szalay A. S., 1993, ApJ, 412, 64

Lima M., Cunha C. E., Oyaizu H., Frieman J., Lin H., Sheldon E. S., 2008, MNRAS, 390, 118

Linder E. V., 2005, PRD, 72, 043529

Myers A. D., Brunner R. J., Nichol R. C., Richards G. T., Schneider D. P., Bahcall N. A., 2007, ApJ, 658, 85

Myers A. D., Brunner R. J., Richards G. T., Nichol R. C., Schneider D. P., Vanden Berk D. E., Scranton R., Gray A. G., Brinkmann J., 2006, ApJ, 638, 622

Nock K., Percival W. J., Ross A. J., 2010, MNRAS, 407, 520

Norberg P., Baugh C. M., Gaztañaga E., Croton D. J., 2009, MNRAS, 396, 19

Okumura T., Matsubara T., Eisenstein D. J., Kayo I., Hikage C., Szalay A. S., Schneider D. P., 2008, ApJ, 676, 889

Oyaizu H., Lima M., Cunha C. E., Lin H., Frieman J., Sheldon E. S., 2008, ApJ, 674, 768

Padmanabhan N., et al., 2007, MNRAS, 378, 852

Percival W. J., Cole S., Eisenstein D. J., Nichol R. C., Peacock J. A., Pope A. C., Szalay A. S., 2007, MNRAS, 381, 1053

Percival W. J., et al., 2010, MNRAS, 401, 2148

Raccanelli A., Samushia L., Percival W. J., 2010, MNRAS, 409, 1525

Ross A. J., Percival W. J., Crocce M., Cabré A., Gaztanaga E., 2011, ArXiv e-prints astro-ph/1102.0968

Samushia L., Percival W. J., Raccanelli A., 2011, ArXiv e-prints astro-ph/1102.1014

Sánchez A. G., Crocce M., Cabré A., Baugh C. M., Gaztañaga E., 2009, MNRAS, 400, 1643

Sawangwit U., Shanks T., Abdalla F. B., Cannon R. D., Croom S. M., Edge A. C., Ross N. P., Wake D. A., 2009, ArXiv e-prints astro-ph/0912.0511

Song Y., Percival W. J., 2009, JCAP, 10, 4

Thomas S. A., Abdalla F. B., Lahav O., 2010, ArXiv e-prints astro-ph/1012.2272

Thomas S. A., Abdalla F. B., Lahav O., 2011, MNRAS, 412, 1669

Tinker J. L., et al., 2011, ArXiv e-prints astro-ph/1104.1635

York D. G., et al., 2000, AJ, 120, 1579

APPENDIX A: EXCESS POWER FOR $Z > 0.6$

One frequent issue when analyzing the clustering of LRGs is the fact that at the largest scales (e.g. BAO) the amplitude of clustering appears generally high when compared to standard Λ CDM models (Eisenstein et al. (2005); Blake et al. (2007); Padmanabhan et al. (2007); Thomas et al. (2010, 2011); Sawangwit et al. (2009); Okumura et al. (2008); Kazin et al. (2010); Cabré & Gaztañaga (2009); Sánchez et al. (2009); Samushia et al. (2011)). The significance of this mismatch is however uncertain since these scales are expected to be the most sensitive ones to different systematic uncertainties as well as the ones with largest statistical variance.

Within the context of photometric data as in our work, Thomas et al. (2011, 2010) recently found $\sim 2\sigma$ excess in the lowest multipoles of the angular power spectrum of LRGs in the MegaZ catalog of DR7 SDSS. As discussed in Sec. 4 we do not find such a discrepancy in our catalog. More so if one recalls that in configuration space data points are expected to co-vary to some level. Potentially much more worrisome is their finding of $\sim 4\sigma$ excess for the bin $[0.6 - 0.65]$ (see also Blake et al. (2007)). Thomas et al. (2010) performed a series of checks for systematic errors but none was conclusively the source of such an effect what led them to speculate with the possibility that this could be due to the imprint of “new physics”, such as primordial non-Gaussianities, modifications of gravity or clustering dark energy.

In Fourier space this excess may not be prejudicial because it only affect few low- ℓ multipoles that can be cut-out of the analysis (they have the lowest signal-to-noise anyway). When translated to configuration-space this impacts a broad range of scales. Hence it is interesting to see how does the clustering in configuration space looks like at $z \gtrsim 0.6$ to complement the study of Thomas et al. (2011, 2010).

In Fig. A1 we show the measured angular correlation function for our photometric bin $[0.6 - 0.65]$. Evidently the clustering signal does not only show an excess power at BAO scales but is in fact anomalous at all scales (except perhaps $\theta < 0.5^\circ$). On the one hand the number of objects in this bin is small ($\sim 30,000$) and dominates the error budget (shot-noise). On the other hand the correlation is very sensitive to various systematic uncertainties. This is reflected in Fig. A1 : the solid magenta line corresponds to the measured correlation when no cut in galactic latitude of the sample or photo- z quality is imposed. Blue solid line is the result when

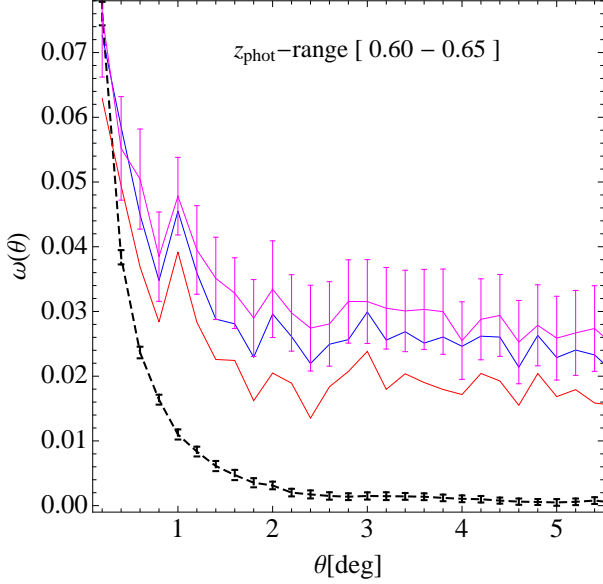


Figure A1. Excess power beyond $z = 0.6$ and sensitivity to systematic effects. Top magenta line corresponds to a mask with no cut in galactic latitude or photo- z quality. Middle blue line correspond to a cut in photo- z quality as discussed in Sec. 2.3. Red solid line corresponds, in addition, to a mask excluding galactic latitude below 25° , see Sec. 2.1. For reference we include the measured correlation in the bin $[0.5-0.6]$. The correlation seems anomalous showing an excess power on all scales and a large sensitivity to various systematic effects.

objects with “bad” photo- z are discarded from the sample (as discussed in Sec. 2.3). Lastly, solid red line is the result when the mask is reduced by leaving out low galactic latitudes $b < 25^\circ$ (to avoid star contamination, see Sec. 2.1). One could continue with more stringent constraints but the signal does not approach the one at lowest bins (shown with black symbols). Displayed error bars in this figure were obtained with jack-knife estimate.

This result signals to unknown systematic uncertainties as the most probable cause for the anomalous shape. One possibility could be an incomplete treatment of the distortions introduced by star contamination. This is generally focused in reducing the fraction of stars to the minimum possible but not to account of the residual clustering signal, as in Sec. 3.2. The contamination by stars results in a change of the mean density across the survey area (and towards the galactic plane). This would impact only the low- ℓ spectra that encodes the mean density information but a broad range of scales in the angular correlation (as shown in Fig. 12). However testing this in Fourier space is beyond the scope of this paper and will be discussed elsewhere.